Annals of Physics 482 (2025) 170209

Contents lists available at ScienceDirect

Annals of Physics

journal homepage: www.elsevier.com/locate/aop

Gravitational weak lensing and shadow radius of black holes in Horndeski gravity: Effects of plasma and scalar modifications

Husanboy Hoshimov [a,*], Shakhzod Orzuev [b,c], Farruh Atamurotov [d,e,f], Ahmadjon Abdujabbarov [g,h]

[a] Fergana State University, Murabbiylar St 19, Fergana 150100, Uzbekistan
[b] New Uzbekistan University, Movarounnahr Street 1, Tashkent 100000, Uzbekistan
[c] Institute of Fundamental and Applied Research, National Research University TIIAME, Kori Niyoziy 39, Tashkent, 100000, Uzbekistan
[d] Kimyo International University in Tashkent, Shota Rustaveli str. 156, Tashkent 100121, Uzbekistan
[e] Research Center of Astrophysics and Cosmology, Khazar University, 41 Mehseti Street, Baku AZ1096, Azerbaijan
[f] Urgench State University, Kh. Alimdjan str. 14, Urgench 220100, Uzbekistan
[g] University of Tashkent for Applied Sciences, Str. Gavhar 1, Tashkent 100149, Uzbekistan
[h] Tashkent State Technical University, Tashkent 100095, Uzbekistan

ARTICLE INFO

Keywords:
Black hole
Gravitational lensing
Modified gravity
Plasma medium

ABSTRACT

In this study, we investigate the impact of Horndeski gravity on the shadow radius and weak gravitational lensing around black holes, with particular focus on how plasma environments influence these phenomena. By considering various plasma distributions, including homogeneous and inhomogeneous models, we examine how gravitational lensing deviates from the vacuum case due to both gravitational effects and plasma-induced inhomogeneities. We find that these deviations can be observed in hot gas environments, such as those within galaxy clusters. Using the photon orbit equations in Horndeski spacetime, we analyze the black hole shadow and weak lensing phenomena. By comparing our theoretical predictions to observational data from the Event Horizon Telescope (EHT) for Sagittarius A*, we constrain key parameters of Horndeski gravity. Additionally, we explore the magnification and positioning of lensed images, and provide detailed calculations of the weak deflection angle and magnification for sources near different galaxies, connecting theoretical models with empirical observations.

1. Introduction

Black holes represent regions in spacetime where the gravitational field is so intense that no form of matter or radiation, including light, can escape their event horizon. They constitute fundamental astrophysical laboratories that rigorously test our theoretical frameworks of gravity, spacetime structure, and fundamental interactions. The study of black holes facilitates the exploration of extreme regimes of gravity, thereby providing critical insights into the nature of spacetime and underpinning the development of theories such as general relativity and quantum field theory. Moreover, black holes play an integral role in galactic formation and cosmic evolution. They are conventionally classified based on their charge and angular momentum into categories such as non-rotating uncharged (Schwarzschild), rotating uncharged (Kerr), rotating charged (Kerr–Newman), and non-rotating charged (Reissner–Nordström) black holes. Recent high-precision observations, notably those documented in [1–3], provide robust empirical evidence confirming the existence of spinning black holes in the M87 galaxy and the Sagittarius A* region.

---

[*] Corresponding author.
E-mail address: hoshimovhusanboy25@gmail.com (H. Hoshimov).

https://doi.org/10.1016/j.aop.2025.170209
Received 9 July 2025; Accepted 31 August 2025

Solutions describing black holes within Horndeski gravity notably depart from the traditional no-hair theorems by allowing the presence of scalar hair, which alters both the structure of the spacetime geometry and the dynamical characteristics of the event horizons [4–6]. Such scalarized black holes have been shown to possess unique signatures that can be observable through gravitational waves, shadows, and lensing effects. Understanding the impact of Horndeski modifications on light propagation is, therefore, crucial for connecting theory with astrophysical data. This metric has been recently utilized to analyze particle dynamics and quasiperiodic oscillations around black holes, providing valuable astrophysical constraints on Horndeski gravity parameters [7–9]. Building upon these foundations, we employ the same metric framework to investigate weak gravitational lensing phenomena, aiming to explore how scalar hair modifies light deflection in the weak-field regime. This makes Horndeski gravity an especially suitable choice for our study, as it allows us to connect well-motivated theoretical deviations from general relativity with measurable observables such as black hole shadow size and weak lensing, which are already constrained by current EHT data for Sgr A* and M87* [10,11]. Gravitational lensing occurs when the gravity of massive objects such as stars or galaxies causes light to bend [12,13]. This bending shifts the apparent position of distant objects in the sky. In some cases, it can produce multiple images of the same object, although these images may appear distorted or stretched. Additionally, gravitational lensing can brighten very faint objects, allowing astronomers to observe farther into space [14,15]. It also alters the shapes of background objects, providing valuable information about the matter located between us and those objects. Light can travel along different paths around the massive body, resulting in slight time delays in its arrival. Due to these effects, gravitational lensing is a crucial tool in astronomy. Researchers use it to study distant celestial bodies, map dark matter, which cannot be seen directly, examine the large-scale structure of the universe, analyze cosmic microwave background radiation, and even detect exoplanets. Moreover, gravitational lensing serves as an important test for Einstein's general relativity theory. By reviewing both historical and recent studies, we gain deeper insights into how this intriguing phenomenon works and its applications in contemporary science [12,16–38]. In gravitational lensing, which is often described using geometric optics, the main effect studied is the bending angle of light rays. However, when plasma is present, its dispersive properties can cause additional color-dependent effects, known as chromatic effects [39]. In this work, we adopt two simple yet astrophysically relevant plasma distributions: a homogeneous model with constant electron density, representative of diffuse, slowly varying environments, and an inhomogeneous model with $\omega_p^2(r) \propto r^{-1}$, which approximates density profiles from spherical accretion flows or isothermal sphere models [39,40]. These choices, widely used in plasma lensing studies [40–42], allow us to capture the qualitative differences between extended uniform plasma and centrally concentrated plasma near compact objects. It is well known that light traveling through a transparent but nonuniform medium moves along curved paths rather than straight lines [43]. Many researchers have explored how plasma influences light propagation in weak gravitational fields using different spacetime models [40–42,44–52]. Gravitational lensing and black hole shadows provide essential insights into the nature of spacetime and the principles of general relativity [53]. Gravitational lensing helps map the distribution of dark matter and acts as a powerful probe into the large-scale structure of the cosmos, serving as a fundamental test of Einstein's theory [54–57]. This work focuses on analyzing weak gravitational lensing and the shadow radius in Horndeski spacetime, considering both uniform and varying plasma environments. By contrasting the adjustments to vacuum lensing resulting from gravitational influences and plasma irregularities, we reveal the impact of plasma on photon paths, shadow features, and magnification of images. Employing data from the Event Horizon Telescope (EHT) for Sgr A*, we impose limits on parameters of modified gravity theories, thereby connecting theoretical predictions with empirical findings and enhancing comprehension of black holes and their immediate surroundings. Additionally, the study explores how plasma (an ionized hot gas pervasive in the universe) affects gravitational lensing through processes such as absorption, scattering, and refraction, which alter the trajectory of light through space.[58–61].

This paper is organized as follows: In Section 2, we provide brief review of Horndeski black hole. In Section 3, we give null geodesic equations in Horndeski spacetime. In Section 4, we probe the Horndeski metric with BH's shadow, In Section 5, we calculate deflection angle and magnification in weak field limit surrounded by plasma. Finally, in Section 6, we summarize obtained results.

2. Brief review of Black Hole solutions in Horndeski gravity

In 1974, Gregory Horndeski introduced what is now known as the Horndeski theory [62]. Since then, it has evolved into a comprehensive and extensively studied framework within the domain of scalar-tensor gravity theories. This theory represents the most general class of models involving a single scalar field that yields second-order field equations, thereby circumventing Ostrogradsky instabilities [63]. It offers a powerful approach for addressing fundamental cosmological issues such as dark energy and the accelerated expansion of the Universe [64]. Furthermore, Horndeski theory provides a robust foundation for exploring black hole (BH) solutions in the context of modified gravity. It facilitates the examination of potential deviations from General Relativity and offers critical insights into the behavior of gravity under extreme physical conditions [65].

The spherically symmetric line element describing a BH solution in Horndeski gravity can be expressed as follows [66–68]:

$$ds^2 = -f(r)dt^2 + \frac{1}{f(r)}dr^2 + r^2\left(d\theta^2 + \sin^2\theta d\phi^2\right) \ , \tag{1}$$

where the radial functions $f(r)$ is given by [67],

$$f(r) = 1 - \frac{2M}{r} - \frac{b^2}{2hgr^2} . \tag{2}$$

Here, M represents the black hole mass. The dimensionless parameters g and b have the same sign, while h is calculated using the formula $\frac{M_P^2}{16\pi}$. The parameter b modulates the non-standard kinetic interaction of the scalar field ϕ with gravity through the term

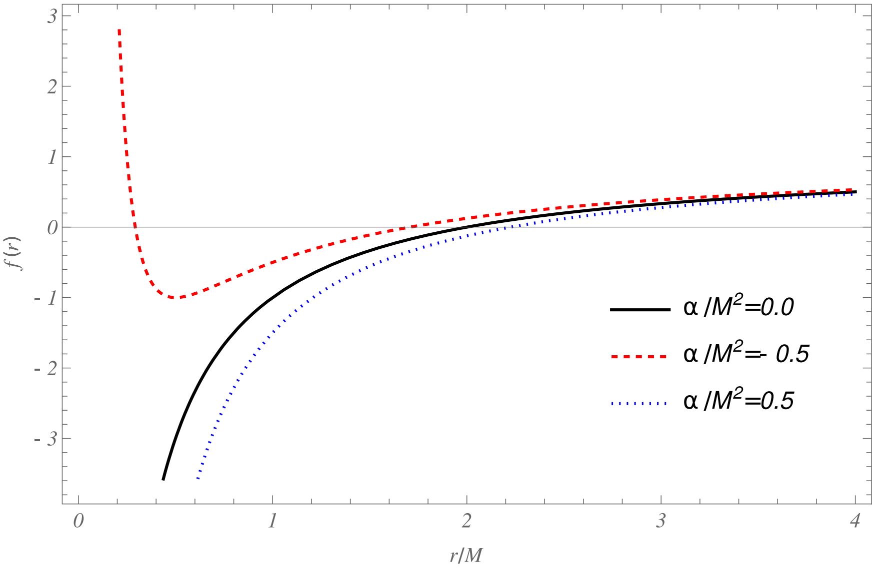

Fig. 1. The plot illustrates the metric function $f(r)$ for varying α/M^2 values, highlighting deviations from the Schwarzschild solution near the event horizon.

$b\sqrt{-X}$, where $X = -\frac{1}{2}(\partial\phi)^2$. It also affects the causal structure and stability of the theory by controlling derivative couplings. The parameter g is coupled with the kinetic term X and determines the magnitude of the canonical kinetic energy of the scalar field, influencing its evolution under gravitational effects. The parameter h, proportional to $M_P^2/(16\pi)$, modulates the Einstein–Hilbert term in the action, allowing the model to reduce to conventional general relativity under specific conditions. For simplicity, we introduce a new parameter $\alpha = \frac{b^2}{2hg}$, treating $\frac{b^2}{2hg}$ as a single entity [cite: horn6]. Thus, we can restate the expression as:

$$f(r) = 1 - \frac{2M}{r} - \frac{\alpha}{r^2}. \tag{3}$$

Fig. 1 illustrates the behavior of the metric function $f(r)$ in Horndeski gravity for different values of the dimensionless coupling parameter α/M^2. Specifically, the function is plotted against the normalized radial coordinate r/M for $\alpha/M^2 = 0$ (black solid), $\alpha/M^2 = -0.5$ (red dashed), and $\alpha/M^2 = 0.5$ (blue dotted). As seen in the figure, negative values of α lead to significant modifications in the near-horizon region, such as the emergence of local extrema and a shift in the event horizon location relative to the Schwarzschild case.

3. Null Geodesic around black hole

The Hamiltonian formulation for a photon moving through a plasma describes how the photon's trajectory is influenced by both gravity and the plasma medium. In this framework, the refractive index n of the plasma modifies the photon's path, leading to additional bending effects, especially in regions of high plasma density. These effects can be included by [69]

$$H(x^\alpha, p_\alpha) = \frac{1}{2}\tilde{g}^{\alpha\beta}p_\alpha p_\beta, \tag{4}$$

The spacetime coordinates are denoted by x^α, while the associated effective metric $\tilde{g}_{\alpha\beta}$ can be represented in the form:

$$\tilde{g}^{\alpha\beta} = g^{\alpha\beta} - (n^2 - 1)u^\alpha u^\beta, \tag{5}$$

Here, n denotes the plasma's refractive index, while p_α and u^β represent the photon's four-momentum and four-velocity, respectively. Eq. (5) follows from the effective metric formalism for photon propagation in a dispersive medium [39,69–71], where the refractive index n depends on the local plasma frequency $\omega_p(r)$. The refractive index n is defined as follows [70]:

$$n^2 = 1 - \frac{\omega_p(r)^2}{\omega(r)^2} \tag{6}$$

In this expression, $\omega_p^2(r) = 4\pi e^2 N(r)/m_e$ represents the plasma electron frequency, where e and m_e denote the charge and mass of the electron, and $N(r)$ is the electron number density. The photon frequency $\omega(r)$, as perceived by a static observer, is determined using the gravitational redshift formula.

$$\omega(r) = \frac{\omega_0}{\sqrt{f(r)}}. \tag{7}$$

At spatial infinity, the frequency ω_0 is constant, where $f(\infty)=1$, and it equals $\omega(\infty)=-p_t$, which represents the photon's energy measured at infinity [71]. For light to propagate in plasma, its frequency must surpass the plasma frequency. Accordingly, Eq. (6) remains valid only if the ratio ω_p/ω is less than one. If this condition is violated, photon propagation ceases. Furthermore, when $\omega_0 \approx \omega$, the deflection angle in plasma exceeds that in vacuum considerably, as shown by $\alpha \gg 2R/b$, where b is the impact parameter. Applying Eqs. (4) and (6) along with the relation $x^\alpha = \delta H/\delta p_\alpha$, the components of the photon's four-velocity vector in the equatorial plane $(\theta = \pi/2, ; p_\theta = 0)$ can be expressed as follows

$$\dot{t} \equiv \frac{\mathrm{d}t}{\mathrm{d}\lambda} = \frac{-p_t}{f(r)}, \tag{8}$$

$$\dot{r} \equiv \frac{\mathrm{d}r}{\mathrm{d}\lambda} = p_r f(r), \tag{9}$$

$$\dot{\phi} \equiv \frac{\mathrm{d}\phi}{\mathrm{d}\lambda} = \frac{p_\phi}{r^2}. \tag{10}$$

From Eqs. (9) and (10), we derive an equation for the phase trajectory of light.

$$\frac{\mathrm{d}r}{\mathrm{d}\phi} = \frac{\dot{r}}{\dot{\phi}} = \frac{f(r) r^2 p_r}{p_\phi}. \tag{11}$$

Using the constraint $H=0$ for the photon motion, we can get following equation

$$\frac{\mathrm{d}r}{\mathrm{d}\phi} = \pm r\sqrt{f(r)}\sqrt{h^2(r)\frac{\omega_0^2}{p_\phi^2} - 1}, \tag{12}$$

where we define [71]

$$h^2(r) \equiv r^2\left[\frac{1}{f(r)} - \frac{\omega_p^2(r)}{\omega_0^2}\right]. \tag{13}$$

To determine the radius r_{ph} of the photon sphere, which corresponds to a circular light orbit around a black hole, one must solve the following equation [71].

$$\left.\frac{\mathrm{d}(h^2(r))}{\mathrm{d}r}\right|_{r=r_{ph}} = 0 \tag{14}$$

Different configurations of plasma distribution and their effects will be considered in the sections that follow.

3.1. Homogeneous plasma

In our analysis, we explore two specific functional forms for $\omega_p(r)$. First we use a homogeneous model with constant $\omega_p(r)$, representing environments where the electron density varies slowly over the photon path, such as in extended diffuse plasma. For this case Eq. (14) has been numerically analyzed. The corresponding plot is shown in Fig. 2. It is evident that increasing the spacetime parameter results in a larger photon orbit radius, and the effect of plasma is to further expand the photon sphere.

3.2. Inhomogeneous plasma

We are currently examining photon spheres in an inhomogeneous plasma, where the plasma frequency must adhere to a straightforward power-law relationship [40,72],

$$\omega_p^2(r) = \frac{z_0}{r}, \tag{15}$$

where z_0 is the free parameter. This approximates density distributions in spherical accretion flows and isothermal spheres [40, 72]. To examine the primary features of the power-law model, we restrict ourselves to this case: $\omega_p^2(r) \sim \frac{1}{r}$ [72]. 2 figure illustrates how the normalized photon sphere radius r_{ph}/M varies with the spacetime parameter α/M^2 under two different plasma environments: homogeneous (left panel, where $\omega_p^2 = \text{const}$) and inhomogeneous (right panel, where $\omega_p^2(r) = z_0/r$). In both scenarios, an increase in the plasma parameter leads to a noticeable growth in the photon sphere radius. These results demonstrate that the presence of plasma enhances photon deflection compared to the vacuum case ($\omega_p^2 = 0$), with the effect being more significant for higher plasma densities. Consequently, distinguishing between homogeneous and non-homogeneous plasma configurations near black holes based solely on their shadow images remains a considerable challenge. Having derived the key equations governing photon orbits and the photon sphere in Horndeski gravity, we now turn our attention to their observable consequences. In particular, we examine how these theoretical predictions compare to the observed black hole shadows and weak gravitational lensing in various astrophysical environments

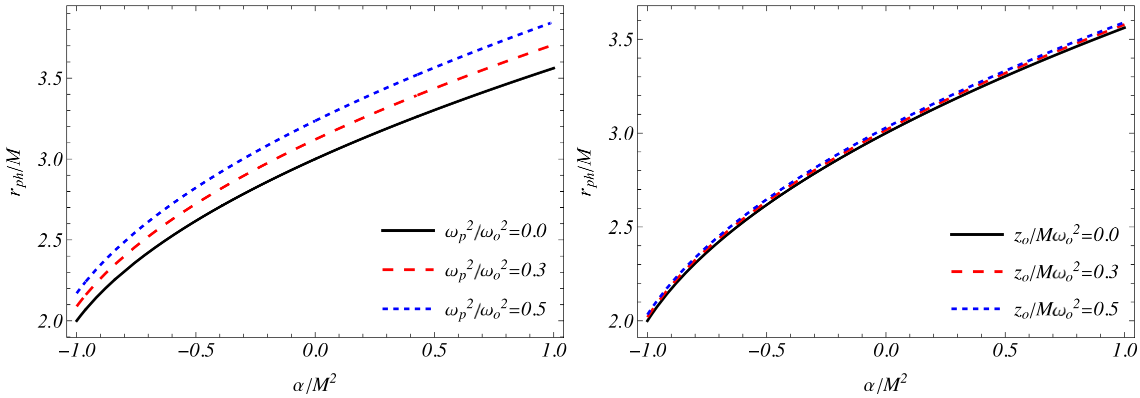

Fig. 2. This graph illustrates the relationship between the radius of the photon sphere r_{ph}/M and the parameter α frequency in a homogeneous (left panel) and inhomogeneous(right panel) with different values of $\omega_p^2 = const$.

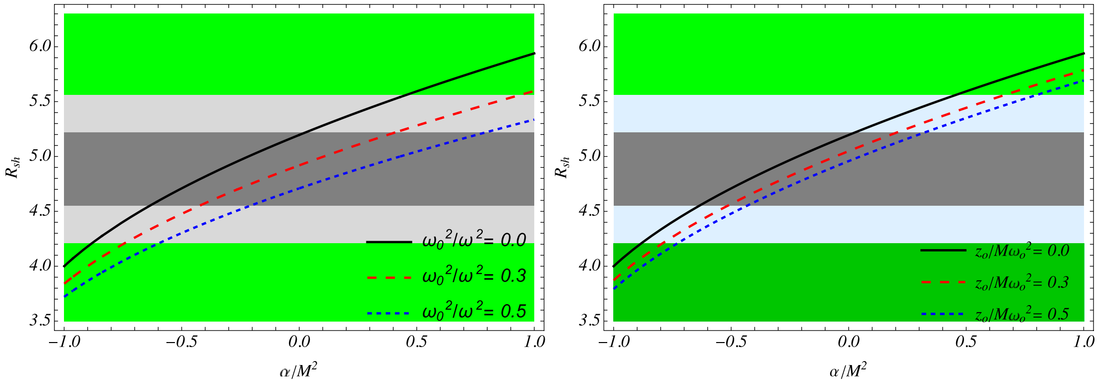

Fig. 3. Illustrations of the radius of the shadow of the black hole as a function of the parameter α for the different $\omega_p^2 = z_0/r$.

4. Analysis of black hole shadows in the presence of a plasma medium

In this part of the study, we explore the behavior of the black hole shadow radius under the Horndeski gravity framework, accounting for spatially constant and variable plasma profiles. The angular size of the shadow, denoted by α_{sh}, is determined via geometric considerations [41,71]

$$\sin^2\alpha_{sh} = \frac{h^2(r_p)}{h^2(r_0)} = \frac{r^2[\frac{1}{f(r_p)} - \frac{\omega_p^2(r_p)}{\omega_0^2}]}{r_0^2[\frac{1}{f(r_0)} - \frac{\omega_p^2(r_0)}{\omega_0^2}]}, \tag{16}$$

the parameters r_0 and r_p correspond to the positions of the distant observer and the photon sphere. Under the assumption of a far-away observer, the black hole shadow radius can be approximated analytically [71]

$$R_{sh} \approx r_0 \sin\alpha_{sh} = \sqrt{r_p^2\left[\frac{1}{f(r_p)} - \frac{\omega_p^2(r_p)}{\omega_0^2}\right]}. \tag{17}$$

This is based on the fact that $h(r) \to r$, which follows from Eq. (13) at spatial infinity for both models of plasma. For vacuum $\omega(r) \equiv 0$, we recover the radius of the Schwarzschild black hole shadow, $R_{sh} = 3\sqrt{3}M$ when $r_p = 3M$. The radius of the black hole shadow is illustrated for different values of α/M^2 is displayed in Fig. 3 (left panel) for the homogeneous plasma. Furthermore, we investigate an inhomogeneous plasma with $\omega_p^2(r) = z_0/r$ in Eq. (15). From Fig. 3 right panel, one can see that due to the presence of plasma, the black-hole shadow radius decreases.

To constrain these parameters, we use the deviations of the angular diameter of the shadow from the Schwarzschild prediction as reported by the EHT. Specifically, the EHT Collaboration provides model-independent measurements of the deviation parameter $\delta = R_{sh}/R_{sh,schw} - 1$, where θ_{sch} is the expected shadow radius for a Schwarzschild black hole. For M87, the deviation is given as $\delta = -0.01 \pm 0.17$ at (1σ) confidence, while for Sgr A, it is $\delta = -0.06 \pm 0.065$ at the 1σ level and $\delta = -0.06 \pm 0.13$ at the 2σ confidence level [2,3]. These plots are intended to assess whether specific black hole spacetime configurations remain consistent with the latest observational data from the Event Horizon Telescope (EHT), particularly for Sagittarius A* (Sgr A*).

The EHT collaboration has reported that the angular size of the shadow of Sgr A* deviates from the Schwarzschild prediction by $\delta = R_{sh}/R_{sh},\mathrm{schw} - 1$, which indicates a reduction in the shadow radius compared to the expectation from general relativity for a Schwarzschild black hole. This constraint defines the allowed parameter space for any alternative or modified gravity models. The black horizontal band in both panels corresponds to the 1σ allowed region from the EHT observation. This is the range where the predicted shadow radius R_{sh} matches the EHT data within one standard deviation. The light gray or light blue regions represent the 2σ confidence level, allowing a broader but still observationally acceptable parameter space.

The green regions are excluded by the EHT observations, as they correspond to predicted shadow radii that deviate significantly (beyond 2σ) from the observed value.

The black, red dashed, and blue dotted curves correspond to theoretical predictions for R_{sh} as a function of α/M^2, under different values of the parameters ω_p^2/ω_0^2 (left panel) and $z_0/(M\omega_0^2)$ (right panel). These parameters can be interpreted as characterizing various coupling strengths or field configurations in the black hole solution.

Interpretation and Constraint Results From both panels, it is evident that the shadow radius R_{sh} generally increases with the parameter α/M^2. However, the degree of increase and whether the theoretical curve passes through the allowed observational region strongly depends on the values of ω_p^2/ω_0^2 and $z_0/(M\omega_0^2)$. In the left panel, we see that for $\omega_p^2/\omega_0^2 = 0$ (black curve), the model remains within the 1σ confidence region only for a relatively narrow range of α/M^2. For higher values of ω_p^2/ω_0^2, the curves shift downward, and for some values of α/M^2, they fall entirely into the excluded (green) region.

Similarly, in the right panel, the increase in $z_0/(M\omega_0^2)$ shifts the shadow radius downward. Only for certain values of α/M^2 does the curve remain inside the 1σ or 2σ allowed regions.

Thus, the black region in both panels represents the parameter space where the predicted shadow radius is consistent with EHT observations of Sgr A*. These regions define the viable range of α/M^2 for each choice of coupling parameters and can be interpreted as observational bounds on the theoretical model.

Conclusion This figure demonstrates that the black hole model in Horndeski theory can be consistent with the observed shadow of Sgr A*, but only for specific combinations of parameters α/M^2, ω_p^2/ω_0^2 and $z_0/(M\omega_0^2)$. Large deviations from these values are ruled out by the EHT data. The analysis thus provides a way to observationally constrain the parameter space of the theory using current black hole imaging results.

5. Weak gravitational lensing in a plasma-filled medium

In this section, we investigate the effects of gravitational lensing around a Horndeski black hole embedded in a plasma medium, using the weak-field approximation as the analytical framework [39]

$$g_{\alpha\beta} = \eta_{\alpha\beta} + h_{\alpha\beta}, \tag{18}$$

here, $\eta_{\alpha\beta}$ denotes the background Minkowski metric, and $h_{\alpha\beta}$ designates the metric perturbation, each with their associated properties [39]

$$\eta_{\alpha\beta} = diag(-1, 1, 1, 1), \tag{19}$$

$$h_{\alpha\beta} \ll 1, \qquad h_{\alpha\beta} \to 0 \qquad \text{under} \qquad x^\alpha \to \infty \tag{20}$$

$$g^{\alpha\beta} = \eta^{\alpha\beta} - h^{\alpha\beta}, \quad h^{\alpha\beta} = h_{\alpha\beta}. \tag{21}$$

Next, we analyze how a surrounding plasma modifies the bending angle of light rays. In a plasma environment, the deflection angle is given by [39,45]

$$\hat{\alpha}_i = \pm\frac{1}{2}\int_{-\infty}^{\infty}\left[\left(h_{33,i} + \frac{\omega^2}{\omega^2 - \omega_e^2}h_{00,i} - \frac{K_e}{\omega^2 - \omega_e^2}\omega^2 N_{,i}\right)\right]\mathrm{d}z. \tag{22}$$

$N(x^i)$ indicates the number density of the particles in the plasma around the black hole and $K_e = 4\pi e^2/m_e$ is a constant parameter. The signs ± of $\hat{\alpha}_i$ indicate deflection towards or away from the central object, respectively. At large distances, the black hole metric can be approximated as

$$\mathrm{d}s^2 = \mathrm{d}s_0^2 + h_{00}\mathrm{d}t^2 + h_{11}\mathrm{d}r^2, \tag{23}$$

The line element is given by $\mathrm{d}s^2 = -\mathrm{d}t^2 + \mathrm{d}r^2 + r^2(\mathrm{d}\theta^2 + \sin^2\theta\mathrm{d}\phi^2)$ and R_s is radius of Schwarzschild. In the Cartesian coordinates the components $h_{\alpha\beta}$ can be given as

$$h_{00} = \left(\frac{R_s}{r} + \frac{\alpha}{r^2}\right), \tag{24}$$

$$h_{jk} = \left(\frac{R_s}{r} + \frac{\alpha}{r^2}\right)n_j n_k, \tag{25}$$

$$h_{33} = \left(\frac{R_s}{r} + \frac{\alpha}{r^2}\right)\cos^2 x, \tag{26}$$

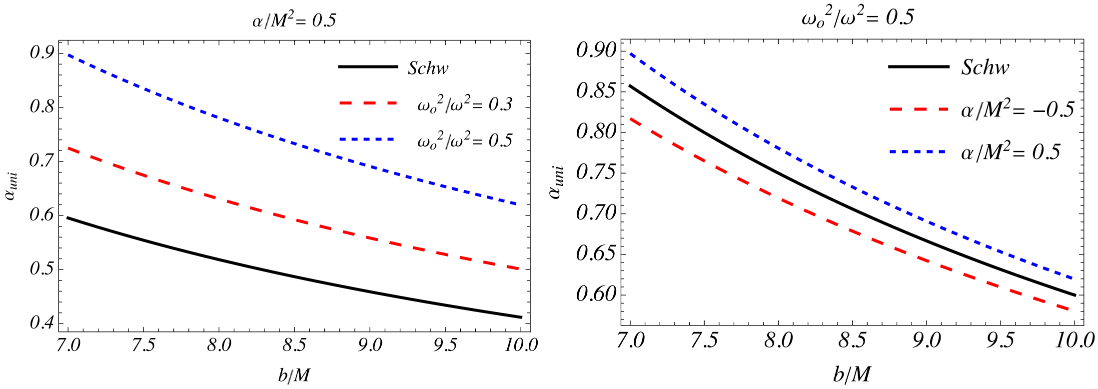

Fig. 4. The variation of deflection angle with impact parameter. In the left panel, higher plasma density increases the deflection. In the right panel, larger α/M^2 enhances the bending effect.

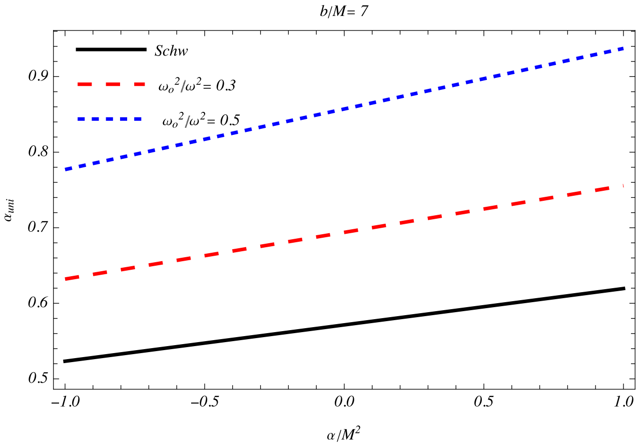

Fig. 5. The figure shows how α/M^2 depends on b/M. In stronger plasma, the value of α increases more quickly.

given that $\cos x = \frac{z}{\sqrt{b^2+z^2}}$ and $r = \sqrt{b^2 + z^2}$, where b denotes the impact parameter representing the minimum distance between the photon trajectory and the black hole, these relations allow us to systematically compute the deflection of light under various plasma distributions.

5.1. Uniform plasma

First, we look at a uniform plasma where ω_0^2 is constant. In this situation, the refractive index does not change with position, so its effect on light bending can be ignored. By integrating Eq. (22), we find the result for the deflection angle

$$\hat{\alpha}_{uni} = \frac{R_s}{b}\left(1 + \frac{1}{1 - \frac{\omega_0^2}{\omega^2}}\right) + \frac{\pi\alpha}{4b^2}\left(1 + \frac{2}{1 - \frac{\omega_0^2}{\omega^2}}\right) \tag{27}$$

Fig. 4 shows how the total deflection angle α_{total} changes with the impact parameter b/M in the case of uniform plasma, where ω_0^2 is constant. In the left panel, for fixed $\alpha/M^2 = 0.5$, a higher plasma frequency ratio ω_0^2/ω^2 leads to more bending. In the right panel, for fixed $\omega_0^2/\omega^2 = 0.5$, increasing α/M^2 causes stronger light deflection. Both cases are compared to the standard Schwarzschild result. Fig. 5 illustrates how the coupling parameter α/M^2 changes depending on the impact parameter b/M. The graph shows that higher impact parameters require larger values of α, and this effect becomes stronger when plasma density increases. The black solid line shows the Schwarzschild case for comparison.

5.2. Singular isothermal sphere

The Singular Isothermal Sphere (SIS) is the most appropriate model to analyze the properties of a gravitational lens photon. It was mainly applied to study the features of lenses and clusters. In general, the SIS is a spherical gas cloud with infinite density at

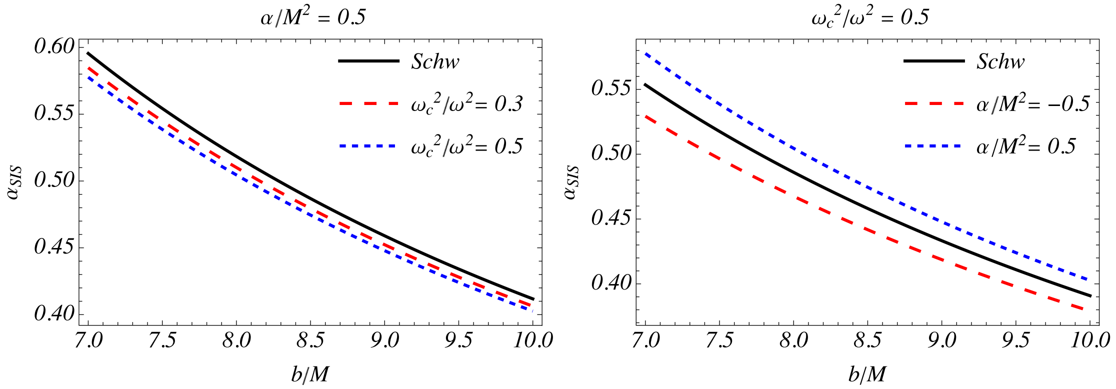

Fig. 6. This figure shows how $\hat{\alpha}_{\rm SIS}$ varies with b/M for different α/M^2 and ω_c^2/ω^2 values.

its center. The density distribution of an SIS is written as [39,51]

$$\rho(r)=\frac{\sigma_v^2}{2\pi r^2} \tag{28}$$

where σ_v^2 implies to a one-dimensional velocity. The plasma distribution is given by the following analytical dispersion relation [39, 51]

$$N(r)=\frac{\rho(r)}{\kappa m_p}, \tag{29}$$

here, m_p denotes the mass of the proton, and k is a dimensionless constant typically associated with the dark matter component of the universe. Using this, the plasma frequency takes the following form:

$$\omega_e^2=K_eN(r)=\frac{K_e\sigma_v^2}{2\pi\kappa m_p r^2}. \tag{30}$$

Taking into account the aforementioned properties of the SIS model, we calculate the deflection angle of light, denoted by $\hat{\alpha}_{SIS}$, which can be expressed as the following equation

$$\hat{\alpha}_{SIS}=\left(\frac{2R_s}{b}-\frac{3\pi\alpha}{4b^2}\right)+\frac{R_s^2\omega_c^2}{b^2\omega^2}\left(\frac{2}{3\pi b}-\frac{1}{2}\right) \tag{31}$$

where ω_c^2 is an additional plasma constant, defined by the following analytical expression. [51]

$$\omega_c^2=\frac{K_e\sigma_v^2}{2\pi\kappa m_p R_s^2} \tag{32}$$

The variation of the deflection angle $\hat{\alpha}_{\rm SIS}$ with respect to the impact parameter b/M is presented in Fig. 6, where different values of the coupling parameter α/M^2 and the plasma constant ratio ω_c^2/ω^2 are considered. In the left panel, for fixed $\alpha/M^2=0.5$, the deflection angle decreases as b/M increases, with a more noticeable drop at higher ω_c^2/ω^2. In the right panel, with $\omega_c^2/\omega^2=0.5$ held constant, increasing α/M^2 leads to greater deflection in comparison to the Schwarzschild case.Fig. 7 shows how the deflection angle $\hat{\alpha}_{\rm SIS}$ depends on the coupling parameter α/M^2 for a fixed impact parameter $b/M=7$. The plot indicates that the deflection angle increases with higher values of α/M^2. Additionally, the figure demonstrates that at greater plasma constant ratios ω_c^2/ω^2, the deflection is slightly weaker for the same α/M^2, compared to the Schwarzschild case shown in black.

5.3. Non-singular isothermal sphere

Next, we turn our attention to the analysis of photon motion in the field of a non-singular isothermal sphere (NSIS), which presents a more physically realistic and applicable structure for our investigation. Unlike the SIS model, this plasma scenario avoids the singularity by incorporating a finite-sized core at the center of the gas distribution, where the density profile is given by the following expression

$$\rho(r)=\frac{\sigma_v^2}{2\pi(r^2+r_c^2)}=\frac{\rho_o}{1+\frac{r^2}{r_c^2}};\qquad \rho_0=\frac{\sigma_v^2}{2\pi r_c^2}, \tag{33}$$

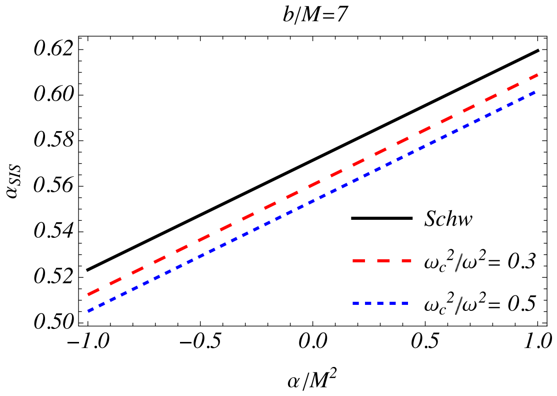

Fig. 7. This figure shows how $\hat{\alpha}_{\mathrm{SIS}}$ changes with α/M^2 at fixed $b/M = 7$ and different plasma levels.

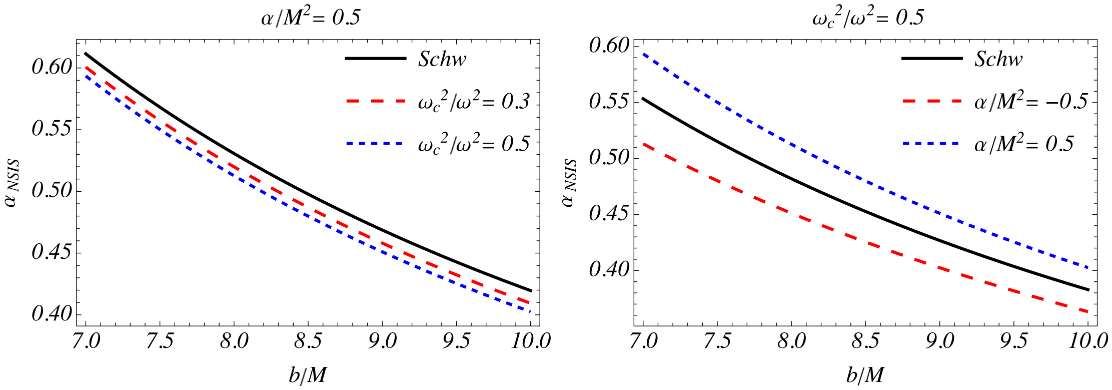

Fig. 8. Plots of a variation of $\hat{\alpha}_{N_{sis}}$ depending on impact parameter b in various Q/M (left panel) and γ (right panel) parameters depending on $\frac{\omega_0^2}{\omega^2}$.

here, the core radius is denoted by r_c. In the NSIS framework, the plasma concentration derived from Eq. (29) can be expressed as follows

$$N(r) = \frac{\sigma_v^2}{2\pi k m_p(r^2 + r_c^2)} \tag{34}$$

We obtain the plasma frequency from Eqs. (30), (32), and (34) in the following form

$$\omega_c^2 = \frac{K_e \sigma_v^2}{2\pi\kappa m_p(r^2 + r_c^2)} \tag{35}$$

After analyzing the data, we can use the following formulas for the deflection angle in the NSIS model (see Fig. 9).

$$\begin{aligned}\hat{\alpha}_{NSIS} = {} & \frac{2R_s}{b} + \alpha\left(\frac{5\pi}{4b^2} + \frac{\omega_c^2 R_s^2 b}{\omega^2 r_c^4\sqrt{b^2 + r_c^2}} + \frac{R_s^2\omega_c^2(r_c^2 - 2b^2)}{2b^2\omega^2 r_c^4}\right) \\ & + R_s^2\frac{\omega_c^2}{\omega^2}\left(\frac{R_s}{\pi b r_c^2} - \frac{b}{2(b^2 + r_c^2)^{\frac{3}{2}}} - \frac{bR_s\tanh^{-1}\frac{r_c}{\sqrt{b^2+r_c^2}}}{\pi r_c^2\sqrt{b^2 + r_c^2}}\right)\end{aligned} \tag{36}$$

Figs. 8 and 9 illustrate the behavior of the deflection angle $\hat{\alpha}_{\mathrm{NSIS}}$ in the NSIS model. The 8 figure shows how $\hat{\alpha}_{\mathrm{NSIS}}$ decreases with increasing impact parameter b/M under different values of α/M^2 and ω_c^2/ω^2, while the second figure demonstrates its growth with increasing α/M^2 for fixed $b/M = 7$. In both cases, higher plasma ratios result in slightly reduced deflection compared to the Schwarzschild baseline [73]. As illustrated in Fig. 10, the deflection angle α as a function of b/M is evaluated for four scenarios: vacuum, uniform plasma, SIS, and NSIS models. Among them, the uniform plasma shows the highest deflection, while the NSIS yields the lowest. The SIS curve lies slightly above the NSIS, and both remain below the vacuum case, indicating that the presence and distribution of plasma significantly affect the bending angle, with uniform plasma producing the most pronounced deviation from the vacuum case.

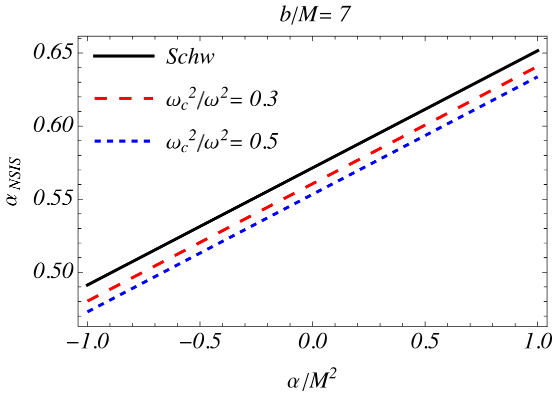

Fig. 9. This figure illustrates a variation of $\hat{\alpha}_{N sis}$ with respect to the charge of black hole Q/M (left panel) and γ (right panel) parameter in different plasma frequency $\frac{\omega_0^2}{\omega^2}$.

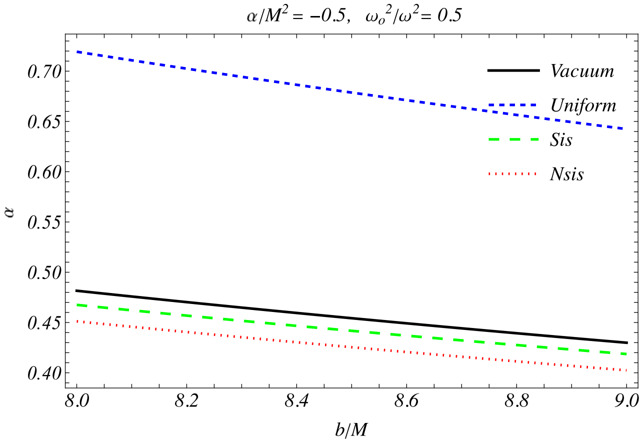

Fig. 10. Comparison of light bending $\hat{\alpha}_b$ as a function of the impact parameter b. The fixed parameters are used as the following $\frac{\omega_0^2}{\omega^2} = 0.5, \frac{\omega_c^2}{\omega^2} = 0.5, r_c = 3$.

5.4. Lens equation and magnification

This part focuses on the influence of gravitational lensing on observed brightness, especially in the context of plasma. In particular, we consider how a uniform plasma medium modifies the magnification of a background light source. The deflection angle $\hat{\alpha}$, introduced in previous sections, is used in the analysis. The lensing configuration, shown in Fig. 11, includes the source, a black hole acting as a lens, and the observer. To evaluate how much the image of the source is magnified, we employ the lens equation, which links the angular position of the source β, the image angle θ, and the relevant distances D_s and D_{ls}, together with the deflection angle. [20,22,74–76]:

$$\theta D_s = \beta D_s + \hat{\alpha} D_{ls}. \tag{37}$$

We can approximate the $b \approx D_d\theta$ relation in weak gravity. After that, we have the following expression.

$$\beta = \theta - \frac{D_{ds}}{D_s}\hat{\alpha}. \tag{38}$$

By substituting Eq. (27) into Eq. (38) within a homogeneous plasma context, we obtain a cubic equation in terms of θ.

$$a\theta^3 + b\theta^2 + c\theta + d = 0, \tag{39}$$

where

$$a = 1, \; b = -\beta, \; c = -\frac{M}{D_d}\left(\frac{1}{1-\frac{\omega_0^2}{\omega 2}} + 1\right),$$

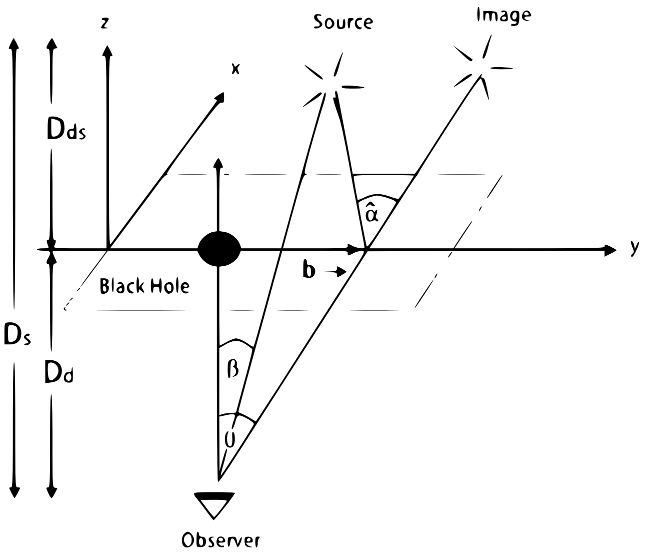

Fig. 11. Schematic view of the gravitational lensing system.

$$d = \frac{\pi\alpha}{8}\frac{M^2}{D_d^2}\left(1+\frac{2}{1-\frac{\omega_0^2}{\omega2}}\right). \tag{40}$$

After creating new variable $\theta = y - \frac{b}{3a}$, we can convert Eq. (39) to this equation [77]

$$y^3 + py + q = 0, \tag{41}$$

where

$$p = \frac{c}{a} - \frac{b^2}{3a^2};\ q = \frac{2b^3}{27a^3} - \frac{bc}{3a} + \frac{d}{a}. \tag{42}$$

It is better to use the Einstein ring θ_E, which is provided below, instead of M/D_d.

$$\theta_E = \sqrt{\frac{2R_s D_{ds}}{D_s D_d}}\ . \tag{43}$$

Then we find the solution to Eq. (41), as described in [78–80].

$$x = 2s^{1/3}\cos\frac{\phi + 2k\pi}{3}, \tag{44}$$

where

$$s = \sqrt{-\frac{p^3}{27}}\ ,\ \ \phi = \arccos\left(-\frac{q}{2s}\right). \tag{45}$$

The total magnification of the images is calculated by the ratio of the observer's solid angles to the source, summed for each image. In the weak field approximation, the total magnification, represented as μ_Σ, is approximately given by [44].

$$\mu_\Sigma = \frac{I_{\rm tot}}{I_*} = \sum_k \left|\left(\frac{\theta_k}{\beta}\right)\left(\frac{{\rm d}\theta_k}{{\rm d}\beta}\right)\right|,\quad k = 1, 2, \dots, n \tag{46}$$

The magnification of the images has three components: two ordinary images and relativistic images caused by the parameter ϵ. Here, θ_k is defined as $x + \beta/3$.

By using some mathematical calculations we can obtain numerical expression for total magnification of image. Fig. 12 illustrates the behavior of the total magnification $\mu_{\rm tot}$ and its individual components as functions of the source position β for different plasma densities, with a fixed coupling parameter $\alpha/M^2 = 0.1$. In the left panel, it is evident that increasing the plasma frequency ratio ω_0^2/ω^2 enhances the total magnification, especially for small values of β. The right panel presents the normalized contributions of the individual images to the total magnification. It shows that as β grows, the first image becomes dominant, while the secondary and tertiary contributions diminish. The inset highlights the behavior of the third image near the lensing axis. In Fig. 13, the variation of the total magnification $\mu_{\rm tot}$ as a function of the position of the source β for different values of the coupling parameter α/M^2, under a fixed plasma frequency ratio $\omega_0^2/\omega^2 = 0.75$. The plot indicates that larger values of α/M^2 result in greater magnification, particularly for small angular separations. The effect gradually decreases as β increases.

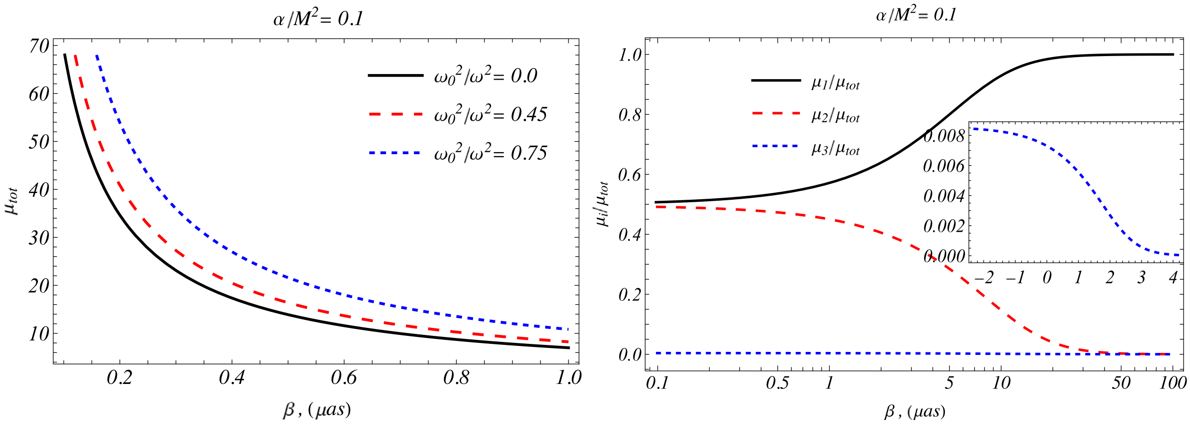

Fig. 12. This figure presents the variation of total magnification μ_{tot} (left panel) and the normalized contributions of individual images (right panel) as functions of the source position β, for different plasma densities and fixed coupling parameter $\alpha/M^2 = 0.1$.

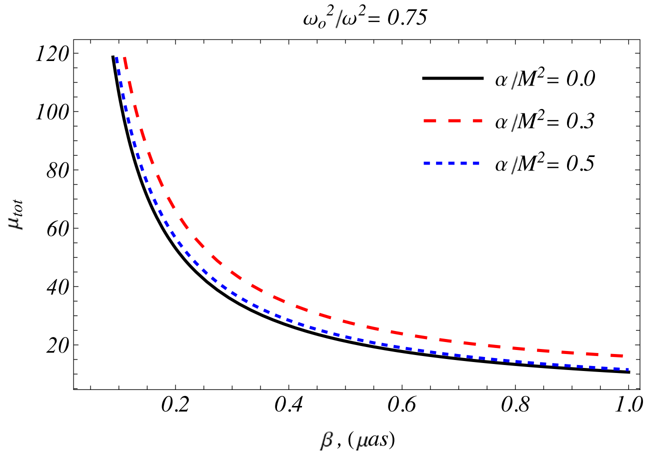

Fig. 13. This figure shows how the total magnification μ_{tot} varies with the source position β for different values of the coupling parameter α/M^2, while the plasma frequency ratio is fixed at $\omega_0^2/\omega^2 = 0.75$. Larger α/M^2 increases magnification at small β.

Table 1

This graph compares the magnification rates of images in uniform plasma and vacuum scenarios. The table uses $M/D_d = 2.26 \cdot 10^{-11}$, corresponding to the supermassive black hole at the Milky Way's center. The parameters include $\beta = 1\,\mu as$, $\alpha/M^2 = 0.5$, and $D_s/D_{ds} = 2$. These values are sourced from [22].

$\mu_n/\mu_n{}^{\text{vac}}$	ω_0^2/ω^2=0.1	ω_0^2/ω^2=0.5	ω_0^2/ω^2=0.9	μ_n^{vac}
$\mu_1/\mu_1{}^{\text{vac}}$	1.02349	1.19294	2.15855	3.88937
$\mu_2/\mu_2{}^{\text{vac}}$	1.03162	1.25971	2.55952	−2.88937
$\mu_3/\mu_3{}^{\text{vac}}$	0.99818	0.91464	0.374768	$-6.52382 \cdot 10^{-18}$

In Table 1, the magnification ratios μ_n/μ_n^{vac} are compared for three individual images under uniform plasma and vacuum conditions. The values are provided for different plasma densities (ω_0^2/ω^2), using parameters specific to the Milky Way's supermassive black hole. The results indicate that plasma significantly affects magnification, particularly at higher densities. Table 2 presents these values for various galaxies.

6. Conclusion

In this paper, we have studied the black hole within Horndeski theory of gravity by examining null geodesics, shadows, and weak gravitational lensing in both homogeneous and inhomogeneous plasma environments. From the above calculations, we can conclude as follows:

Table 2

Table 2 provides angular positions and magnifications of secondary, primary, and relativistic images for supermassive black holes (MDOs) in several galaxies. The data show that primary images dominate in brightness, while relativistic images have extremely small magnifications across all cases. The Milky Way has the highest relativistic contribution. All calculation is done with $\beta = 1(\mu as)$, $\alpha/M^2 = 0.5$ and ω_o^2/ω^2=0.5.

	Secondary$*$		Primary$*$		Relativistic$*$	
MDO in galaxy	θ_{sec}	μ_{sec}	θ_{pri}	μ_{pri}	θ_{rel}	μ_{rel}
Milky Way	−6.77897	3.15666	7.77896	4.15666	$8.70217 \cdot 10^{-6}$	$1.24965 \cdot 10^{-17}$
NGC4649	−3.17786	1.37292	4.17786	2.37292	$2.19094 \cdot 10^{-6}$	$7.92244 \cdot 10^{-19}$
NGC4594	−3.07328	1.32162	4.07328	2.32162	$2.0658 \cdot 10^{-6}$	$7.04219 \cdot 10^{-19}$
NGC3115	−2.92767	1.2503	3.92767	2.2503	$1.89758 \cdot 10^{-6}$	$5.94204 \cdot 10^{-19}$
NGC224(M2)	−2.74398	1.160525	3.74398	2.16052	$1.69534 \cdot 10^{-6}$	$4.74221 \cdot 10^{-19}$
IC1459	−2.63044	1.10515	3.63044	2.10515	$1.5759 \cdot 10^{-6}$	$4.09932 \cdot 10^{-19}$
NGC4374	−2.07365	0.835395	3.07365	1.8354	$1.0518 \cdot 10^{-6}$	$1.82633 \cdot 10^{-19}$
NGC4374(M84)	−2.01236	0.805932	3.01236	1.80593	$1.00035 \cdot 10^{-6}$	$1.65148 \cdot 10^{-19}$

- Testing the null geodesic reveals that photon orbits expand as the parameter α increases. Plasma has a positive effect in both homogeneous and inhomogeneous scenarios.
- Analysis in the weak gravitational field regime reveals that the inclusion of the Horndeski coupling parameter α results in a reduction of light bending relative to General Relativity predictions.
- In the shadow analysis, $R_{\rm sh}$ increases monotonically with α in vacuum, whereas both homogeneous and centrally concentrated plasmas with $\omega_p^2(r) \propto r^{-1}$ shift $R_{\rm sh}$ to smaller values. This α-plasma degeneracy implies that shadow-size constraints should be interpreted jointly with plasma information.
- In the weak-lensing sector, different plasma distributions yield ordered departures from vacuum: a uniform (homogeneous) plasma produces the largest reduction in bending/magnification, SIS gives intermediate changes, and NSIS the smallest, for the same ratio ω_p^2/ω^2.
- The frequency dependence introduced by plasma (chromaticity) leads to image positions and magnifications that vary with observing frequency; in the high-frequency limit ($\omega \gg \omega_p$), our results smoothly recover the achromatic predictions of General Relativity.
- Consistency and outlook: all expressions reduce to the Schwarzschild-vacuum limits as $\alpha \to 0$ and $\omega_p \to 0$, supporting the robustness of our framework. Extending to rotating Horndeski black holes, strong-deflection lensing, and multi-frequency ray tracing against EHT/ngEHT data can further tighten bounds on α and on plasma profiles.
- Also, we have studied the influence of plasma in radius of the shadow. Our constraint showed that allowed values of the parameter α is from approximately -0.88 to 0.46 in 2σ, while these values are $-0.64 \div 0.025$ in 1σ confidence level in the absence of plasma. Due to the possible existence of plasma environment, these parameter range may change.

CRediT authorship contribution statement

Husanboy Hoshimov: Writing – original draft, Visualization, Investigation, Funding acquisition, Formal analysis, Data curation, Writing – review & editing. **Shakhzod Orzuev:** Formal analysis, Investigation, Software, Validation, Visualization. **Farruh Atamurotov:** Conceptualization, Investigation, Methodology, Resources, Supervision, Writing – original draft, Writing – review & editing. **Ahmadjon Abdujabbarov:** Funding acquisition, Investigation, Methodology, Project administration, Resources, Writing – original draft, Writing – review & editing.

Declaration of competing interest

The authors declare that they have no known competing financial interests or personal relationships that could have appeared to influence the work reported in this paper.

Data availability

No data was used for the research described in the article.

References

[1] B.P. Abbott and, et al., Observation of gravitational waves from a binary black hole merger, Phys. Rev. Lett. 116 (2016) 061102, arXiv:1602.03837 [gr-qc].

[2] K. Akiyama, et al., Event Horizon Telescope, First Sagittarius A* event horizon telescope results. I. The shadow of the supermassive black hole in the center of the milky way, Astrophys. J. Lett. 930 (2022) L12, arXiv:2311.08680 [astro-ph.HE].

[3] K. Akiyama, et al., Event Horizon Telescope, First M87 event horizon telescope results. VIII. Magnetic field structure near the event horizon, Astrophys. J. Lett. 910 (2021) L13, arXiv:2105.01173 [astro-ph.HE].

[4] E. Babichev, C. Charmousis, Dressing a black hole with a time-dependent Galileon, J. High Energy Phys. 2014 (2014) 106, arXiv:1312.3204 [gr-qc].

[5] T.P. Sotiriou, S.-Y. Zhou, Black hole hair in generalized scalar-tensor gravity: An explicit example, Phys. Rev. D 90 (2014) 124063, arXiv:1408.1698 [gr-qc].

[6] A. Anabalon, A. Cisterna, J. Oliva, Asymptotically locally AdS and flat black holes in Horndeski theory, Phys. Rev. D 89 (2014) 084050, arXiv:1312.3597 [gr-qc].

[7] J. Rayimbaev, K.F. Dialektopoulos, F. Sarikulov, A. Abdujabbarov, Quasiperiodic oscillations around hairy black holes in Horndeski gravity, Eur. Phys. J. C 83 (2023) 572, arXiv:2307.03019 [gr-qc].

[8] O. Donmez, From low- to high-frequency QPOs around the non-rotating hairy horndeski black hole: Microquasar GRS 1915+105, J. High Energy Astrophys. 45 (2025) 1, arXiv:2408.10102 [astro-ph.HE].

[9] A. Ashraf, A.S. Alqahtani, F. Javed, P. Channuie, A. Cilli, A. Bouzenada, E. Güdekli, M.Y. Malik, Orbital motion and QPOs testing around rotating hairy black holes in horndeski gravity, Phys. Dark Universe 47 (2025) 101725.

[10] Event Horizon Telescope Collaboration, First Sagittarius A* event horizon telescope results. I. The shadow of the supermassive black hole in the center of the milky way, Astrophys. J. Lett. 930 (2022) L12.

[11] Event Horizon Telescope Collaboration, First M87 event horizon telescope results. I. The shadow of the supermassive black hole, Astrophys. J. Lett. 875 (2019) L1.

[12] V. Perlick, Gravitational lensing from a spacetime perspective, Living Rev. Rel. 7 (2004) 9.

[13] A. Einstein, Lens-like action of a star by the deviation of light in the gravitational field, Science 84 (1936) 506.

[14] M. Bartelmann, P. Schneider, Weak gravitational lensing, Phys. Rep. 340 (2001) 291, arXiv:astro-ph/9912508.

[15] T. Treu, Strong lensing by galaxies, Annu. Rev. Astron. Astrophys. 48 (2010) 87.

[16] P. Schneider, J. Ehlers, E.E. Falco, Gravitational lenses, in: Astronomy and Astrophysics Library, Springer-Verlag Berlin Heidelberg, 1992, p. 560.

[17] S. Mao, Astrophysical applications of gravitational microlensing, Res. Astron. Astrophys. 12 (2012) 947, arXiv:1207.3720 [astro-ph.GA].

[18] M. Bartelmann, P. Schneider, Weak gravitational lensing, Phys. Rep. 340 (2001) 291, arXiv:astro-ph/9912508.

[19] M. Bartelmann, Gravitational lensing, Cl. Quant. Grav. 27 (2010) 233001, arXiv:1010.3829 [astro-ph.CO].

[20] K.S. Virbhadra, G.F.R. Ellis, Schwarzschild black hole lensing, Phys. Rev. D 62 (2000) 084003, arXiv:astro-ph/9904193.

[21] K.S. Virbhadra, G.F.R. Ellis, Gravitational lensing by naked singularities, Phys. Rev. D 65 (2002) 103004.

[22] K.S. Virbhadra, Relativistic images of Schwarzschild black hole lensing, Phys. Rev. D 79 (2009) 083004, arXiv:0810.2109 [gr-qc].

[23] B. Puliçe, R.C. Pantig, A. Övgün, D. Demir, Constraints on charged symmergent black hole from shadow and lensing, Cl. Quant. Grav. 40 (2023) 195003, arXiv:2308.08415 [gr-qc].

[24] R.C. Pantig, L. Mastrototaro, G. Lambiase, A. Övgün, Shadow, lensing, quasinormal modes, greybody bounds and neutrino propagation by dyonic ModMax black holes, Eur. Phys. J. C 82 (2022) 1155, arXiv:2208.06664 [gr-qc].

[25] X.-M. Kuang, A. Övgün, Strong gravitational lensing and shadow constraint from M87* of slowly rotating Kerr-like black hole, Ann. Phys. 447 (2022) 169147, arXiv:2205.11003 [gr-qc].

[26] Z. Li, G. Zhang, A. Övgün, Circular orbit of a particle and weak gravitational lensing, Phys. Rev. D 101 (2020) 124058, arXiv:2006.13047 [gr-qc].

[27] A. Övgün, I. Sakallı, J. Saavedra, Weak gravitational lensing by Kerr-MOG black hole and Gauss–Bonnet theorem, Ann. Phys. 411 (2019) 167978, arXiv:1806.06453 [gr-qc].

[28] Y. Kumaran, A. Övgün, Shadow and deflection angle of asymptotic, magnetically-charged, non-singular black hole, Eur. Phys. J. C 83 (2023) 812, arXiv:2306.04705 [gr-qc].

[29] G. Lambiase, L. Mastrototaro, R.C. Pantig, A. Ovgun, Probing Schwarzschild-like black holes in metric-affine bumblebee gravity with accretion disk, deflection angle, greybody bounds, and neutrino propagation, J. Cosmol. Astropart. Phys. 12, 026, arXiv:2309.13594 [gr-qc].

[30] E. Sucu, A. Övgün, The effect of quark–antiquark confinement on the deflection angle by the NED black hole, Phys. Dark Univ. 44 (2024) 101446.

[31] A. Övgün, R.C. Pantig, A. Rincón, 4D scale-dependent Schwarzschild-AdS/dS black holes: study of shadow and weak deflection angle and greybody bounding, Eur. Phys. J. Plus 138 (2023) 192, arXiv:2303.01696 [gr-qc].

[32] R.C. Pantig, A. Övgün, D. Demir, Testing symmergent gravity through the shadow image and weak field photon deflection by a rotating black hole using the M87* and Sgr. A* results, Eur. Phys. J. C 83 (2023) 250, arXiv:2208.02969 [gr-qc].

[33] A. Uniyal, R.C. Pantig, A. Övgün, Probing a non-linear electrodynamics black hole with thin accretion disk, shadow, and deflection angle with M87* and Sgr A* from EHT, Phys. Dark Univ. 40 (2023) 101178, arXiv:2205.11072 [gr-qc].

[34] M. Okyay, A. Övgün, Nonlinear electrodynamics effects on the black hole shadow, deflection angle, quasinormal modes and greybody factors, J. Cosmol. Astropart. Phys. 01 (01) 009, arXiv:2108.07766 [gr-qc].

[35] W. Javed, A. Hamza, A. Övgün, Effect of nonlinear electrodynamics on the weak field deflection angle by a black hole, Phys. Rev. D 101 (2020) 103521, arXiv:2005.09464 [gr-qc].

[36] A. Övgün, I. Sakallı, Testing generalized Einstein–Cartan–Kibble–Sciama gravity using weak deflection angle and shadow cast, Cl. Quant. Grav. 37 (2020) 225003, arXiv:2005.00982 [gr-qc].

[37] A. Davlataliev, B. Narzilloev, I. Hussain, A. Abdujabbarov, B. Ahmedov, Probing the Starobinsky–Bel–Robinson gravity by photon motion around the Kerr-type black hole in non-uniform plasma, Phys. Dark Univ. 42 (2023) 101340.

[38] Y. Pahlavon, F. Atamurotov, K. Jusufi, M. Jamil, A. Abdujabbarov, Effect of magnetized plasma on shadow and gravitational lensing of a Reissner–Nordström black hole, Phys. Dark Universe 45 (2024) 101543, arXiv:2406.09431 [gr-qc].

[39] G.S. Bisnovatyi-Kogan, O.Y. Tsupko, Gravitational lensing in a non-uniform plasma, Mon. Not. R. Astron. Soc. 404 (2010) 1790, arXiv:1006.2321 [astro-ph.CO].

[40] A. Rogers, Frequency-dependent effects of gravitational lensing within plasma, Mon. Not. R. Astron. Soc. 451 (2015) 17.

[41] F. Atamurotov, K. Jusufi, M. Jamil, A. Abdujabbarov, M. Azreg-Aïnou, Axion-plasmon or magnetized plasma effect on an observable shadow and gravitational lensing of a Schwarzschild black hole, Phys. Rev. D 104 (2021) 064053, arXiv:2109.08150 [gr-qc].

[42] A. Hakimov, F. Atamurotov, Gravitational lensing by a non-Schwarzschild black hole in a plasma, Astrophys. Space Sci. 361 (2016) 112.

[43] V.V. Zhelezniakov, Electromagnetic Waves in Space Plasma: Generation and Propagation, Moscow Izdatel Nauka, 1977.

[44] V.S. Morozova, B.J. Ahmedov, A.A. Tursunov, Gravitational lensing by a rotating massive object in a plasma, Astrophys. Space Sci. 346 (2013) 513.

[45] F. Atamurotov, M. Jamil, K. Jusufi, Quantum effects on the black hole shadow and deflection angle in the presence of plasma*, Chin. Phys. C 47 (2023) 035106, arXiv:2212.12949 [gr-qc].

[46] F. Atamurotov, H. Alibekov, A. Abdujabbarov, G. Mustafa, M.M. Aripov, Weak gravitational lensing around bardeen black hole with a string cloud in the presence of plasma, Symmetry 15 (2023) 848.

[47] A. Abdujabbarov, B. Toshmatov, J. Schee, Z. Stuchlík, B. Ahmedov, Gravitational lensing by regular black holes surrounded by plasma, Internat. J. Modern Phys. D 26 (2017) 1741011–1741187.

[48] G.Z. Babar, F. Atamurotov, S. Ul Islam, S.G. Ghosh, Particle acceleration around rotating Einstein-Born–Infeld black hole and plasma effect on gravitational lensing, Phys. Rev. D 103 (2021) 084057, arXiv:2104.00714 [gr-qc].

[49] F. Atamurotov, A. Abdujabbarov, W.-B. Han, Effect of plasma on gravitational lensing by a Schwarzschild black hole immersed in perfect fluid dark matter, Phys. Rev. D 104 (2021) 084015.

[50] F. Atamurotov, S. Shaymatov, P. Sheoran, S. Siwach, Charged black hole in 4D Einstein-Gauss–Bonnet gravity: particle motion, plasma effect on weak gravitational lensing and centre-of-mass energy, J. Cosmol. A. P. 2021 (2021) 045, arXiv:2105.02214 [gr-qc].

[51] G.Z. Babar, F. Atamurotov, A.Z. Babar, Gravitational lensing in 4-D Einstein-Gauss–Bonnet gravity in the presence of plasma, Phys. Dark Universe 32 (2021) 100798.

[52] F. Atamurotov, O. Yunusov, A. Abdujabbarov, G. Mustafa, Gravitational weak lensing of hairy black hole in presence of plasma, New Astron. 105 (2024) 102098.

[53] C.M. Will, The confrontation between general relativity and experiment, Living Rev. Relativ. 17 (2014) http://dx.doi.org/10.12942/lrr-2014-4.

[54] D. Clowe, M. Bradač, A.H. Gonzalez, M. Markevitch, S.W. Randall, C. Jones, D. Zaritsky, A direct empirical proof of the existence of dark matter, Astrophys. J. Lett. 648 (2006) L109.

[55] M. Kilbinger, Cosmology with cosmic shear observations: a review, Rep. Progr. Phys. 78 (2015) 086901.

[56] B. Jain, J. Khoury, Cosmological tests of gravity, Annu. Rev. Nucl. Part. Sci. 60 (2010) 399.

[57] Planck Collaboration, Planck 2018 results. VIII. Gravitational lensing, Astron. Astrophys. 641 (2020) A8.

[58] A. Rogers, Frequency-dependent effects of gravitational lensing within plasma, Mon. Not. R. Astron. Soc. 451 (2015) 17.

[59] X. Er, S. Mao, Effects of plasma on gravitational lensing, Mon. Not. R. Astron. Soc. 437 (2014) 2180.

[60] V.S. Morozova, B.J. Ahmedov, A.A. Tursunov, Gravitational lensing by a rotating massive object in a plasma, Astrophys. Space Sci. 346 (2013) 513.

[61] V. Perlick, O.Y. Tsupko, Calculating black hole shadows: Review of analytical studies, Phys. Rep. 947 (2022) 1.

[62] G.W. Horndeski, Second-order scalar-tensor field equations in a four-dimensional space, Internat. J. Theoret. Phys. 10 (1974) 363.

[63] E. Babichev, C. Charmousis, Dressing a black hole with a time-dependent galileon, J. High Energy Phys. 2014 (2014) 106, arXiv:1312.3204 [gr-qc].

[64] T. Clifton, P.G. Ferreira, A. Padilla, C. Skordis, Modified gravity and cosmology, Phys. Rep. 513 (2012) 1, arXiv:1106.2476 [astro-ph.CO].

[65] T. Kobayashi, Horndeski theory and beyond: a review, Rep. Progr. Phys. 82 (2019) 086901, arXiv:1901.07183 [gr-qc].

[66] E. Babichev, C. Charmousis, A. Lehébel, Asymptotically flat black holes in Horndeski theory and beyond, J. Cosmol. Astropart. Phys. 2017 (2017) 027, arXiv:1702.01938 [gr-qc].

[67] Z. Luo, J. Li, K.-J. He, H. Yu, Shadows, quasinormal modes, and optical appearances of black holes in Horndeski theory, 2024, arXiv e-prints, arXiv:2406.00265 [gr-qc].

[68] M. Zahid, O. Yunusov, C. Shen, J. Rayimbaev, S. Muminov, Shadows and quasinormal modes of rotating black holes in Horndeski theory: Parameter constraints using EHT observations of M87* and Sgr A*, Phys. Dark Universe 47 (2025) 101734.

[69] J.L. Synge, Relativity: The General Theory, Interscience Publishers, New York, 1960.

[70] J.T. Mendonça, J.D. Rodrigues, H. Terças, Axion production in unstable magnetized plasmas, Phys. Rev. D 101 (2020) 051701.

[71] V. Perlick, O.Y. Tsupko, G.S. Bisnovatyi-Kogan, Influence of a plasma on the shadow of a spherically symmetric black hole, Phys. Rev. D 92 (2015) 104031, arXiv:1507.04217 [gr-qc].

[72] X. Er, A. Rogers, Two families of astrophysical diverging lens models, Mon. Not. R. Astron. Soc. 475 (2018) 867, arXiv:1712.06900 [astro-ph.GA].

[73] B. Bezděková, Electromagnetic Waves in Dispersiveand Refractive Relativistic Systems (Master's thesis), Univerzita Karlova, Matematicko-fyzikálnífakulta, Ústav teoretické fyziky, Diplomová práce, vedoucíBičák, Jiří. Praha, 2019.

[74] V. Bozza, Gravitational lensing by black holes, Gen. Relativity Gravitation 42 (2010) 2269, arXiv:0911.2187 [gr-qc].

[75] A. Younas, S. Hussain, M. Jamil, S. Bahamonde, Strong gravitational lensing by Kiselev black hole, Phys. Rev. D 92 (2015) 084042, arXiv:1502.01676 [gr-qc].

[76] M. Azreg-Aïnou, S. Bahamonde, M. Jamil, Strong gravitational lensing by a charged Kiselev black hole, Eur. Phys. J. C 77 (2017) 414, arXiv:1701.02239 [gr-qc].

[77] S. Orzuev, F. Atamurotov, A. Abdujabbarov, A. Abduvokhidov, Weak gravitational lensing of black hole from T-duality in plasma, New Astron. 105 (2024) 102104.

[78] B. Turimov, B. Ahmedov, A. Abdujabbarov, C. Bambi, Gravitational lensing by a magnetized compact object in the presence of plasma, Internat. J. Modern Phys. D 28 (2019) 2040013–2040187, arXiv:1802.03293 [gr-qc].

[79] H. Hoshimov, O. Yunusov, F. Atamurotov, M. Jamil, A. Abdujabbarov, Weak gravitational lensing and shadow of a GUP-modified Schwarzschild black hole in the presence of plasma, Phys. Dark Universe 43 (2024) 101392, arXiv:2312.10678 [gr-qc].

[80] D. Umarov, O. Yunusov, F. Atamurotov, A. Abdujabbarov, S.G. Ghosh, Plasma effects on weak gravitational lensing and shadows of Sen black holes, Chin. Phys. C 49 (2025) 055102.